JACS
JOURNAL OF THE AMERICAN CHEMICAL SOCIETY
Communication
pubs.acs.org/JACS

Zn/MnO_2 Battery Chemistry With H^+ and Zn^{2+} Coinsertion

Wei Sun,[†,‡,∥] Fei Wang,[†,∥] Singyuk Hou,[†] Chongyin Yang,[†] Xiulin Fan,[†] Zhaohui Ma,[†] Tao Gao,[†] Fudong Han,[†] Renzong Hu,[‡] Min Zhu,[*,‡] and Chunsheng Wang[*,†]

[†]Department of Chemical and Bimolecular Engineering, University of Maryland, College Park, Maryland 20740, United States
[‡]School of Materials Science and Engineering, South China University of Technology, Guangzhou 510641, China

Supporting Information

ABSTRACT: Rechargeable aqueous Zn/MnO_2 battery chemistry in a neutral or mildly acidic electrolyte has attracted extensive attention recently because all the components (anode, cathode, and electrolyte) in a Zn/MnO_2 battery are safe, abundant, and sustainable. However, the reaction mechanism of the MnO_2 cathode remains a topic of discussion. Herein, we design a highly reversible aqueous Zn/MnO_2 battery where the binder-free MnO_2 cathode was fabricated by in situ electrodeposition of MnO_2 on carbon fiber paper in mild acidic $ZnSO_4$+$MnSO_4$ electrolyte. Electrochemical and structural analysis identify that the MnO_2 cathode experience a consequent H^+ and Zn^{2+} insertion/extraction process with high reversibility and cycling stability. To our best knowledge, it is the first report on rechargeable aqueous batteries with a consequent ion-insertion reaction mechanism.

Lithium-ion (Li-ion) batteries have taken over the commercial rechargeable battery market due to their high energy density.[1] However, the growing concerns about limited resources, high cost, poor safety, and environment benignity of Li-ion batteries revive aqueous batteries.[2] Rechargeable aqueous Zn/MnO_2 batteries are considered as one of the best alternatives owing to the high abundance and safety of both Zn and MnO_2, as well as the intrinsic nonflammability and the high ionic conductivity of the aqueous electrolyte.[3] However, in alkaline electrolyte, several irreversible byproducts formed on the anode (ZnO or $Zn(OH)_2$) and the cathode ($Mn(OH)_2$, Mn_3O_4, and Mn_2O_3), resulting in severe capacity fading and poor Coulombic efficiencies.[4] Recently, neutral or mild acidic aqueous electrolytes were used in rechargeable aqueous Zn/MnO_2 battery to improve the electrochemical performance.[5] Despite the significant advance in battery performance, the reaction mechanism of the MnO_2 cathode in neutral or mild acidic aqueous electrolytes remains controversial and under debate. Two charge/discharge mechanisms for MnO_2 have been reported. Several experiments demonstrated that the capacity of MnO_2 in neutral or mild acidic aqueous electrolytes is induced by the reversible Zn^{2+} insertion/extraction;[5a,b,6] whereas other experiments supported the reversible H^+ insertion/extraction process.[5c,7] The different mechanism observed in these experiments may be attributed to the difference in crystallographic polymorphs (α, β, γ, δ, λ, and amorphous) and the particle size of MnO_2,[8] which significantly change the ion insertion thermodynamics and kinetics of H^+ and Zn^{2+}.

To better understand the mechanism, we proposed the in situ electrodeposition method to prepare the binder-free nanocrystal MnO_2 cathode, which could minimize the impact of ion insertion kinetics and crystallographic polymorph on the mechanism. The electrodeposition was also motivated by the fact that the Mn dissolution-deposition always happens in the MnO_2 cathode.[7,8] When the concentration of Mn^{2+} ions in the electrolyte increases to a certain level, the dissolved Mn^{2+} ions in the neutral or mild acidic aqueous electrolyte could be electro-oxidized back to manganese oxides (MnO_x) on the cathode and balance the dissolution loss of MnO_2, thus extreme long cycle life of Zn/MnO_2 was reported.[5c] After the repeated charge−discharge cycles, the redeposited MnO_x could be the dominant component instead of the pristine MnO_2.[8a] Therefore, it is important to understand the reaction mechanism of the electrodeposited MnO_2 in the neutral or mild acidic electrolyte, which represent a true mechanism for long cycled MnO_2 cathodes.

In this study, we demonstrated that the electrodeposited MnO_2 experienced the successive H^+ and Zn^{2+} insertion processes with a distinct difference in reaction kinetics during the discharging. The electrodeposited MnO_2 has a nanocrystalline structure, in which the particle size is typically less than 10 nm, providing abundant electrode/electrolyte contact interfaces and reduced ion diffusion path and ensuring that the reaction with slow electrochemical kinetics could also happen. The as-designed Zn/MnO_2 battery delivered an excellent cycling performance with a low capacity decay rate of 0.007% per cycle for 10 000 cycles at a high rate of 6.5 C.

The electrodeposition process is schematically illustrated in Figure 1a. The Mn^{2+} from the $MnSO_4$ solution is oxidized to form the uniform MnO_2 deposited on the surface of the carbon fiber paper (CFP) (inset Figure 1a and Figure S1). Importantly, this synthetic approach provides an intimate direct contact of MnO_2 with the CFP, without the use of any polymer binder or conductive additives. Figure 1b shows the XRD pattern of obtained MnO_2@CFP electrode. All peaks are well indexed to Akhtenskite MnO_2 (JCPDS 30-0820), and their weak and broad feature reveals the typical characteristic of nanocrystalline. As shown in the XPS reuslts (Figure 1c and S2), the electrodeposited MnO_2 exhibits a spin-energy separation of 4.8 eV for the Mn 3s doublet, indicating the Mn in the electrode

Received: May 1, 2017
Published: July 13, 2017

DOI: 10.1021/jacs.7b04471
J. Am. Chem. Soc. 2017, 139, 9775−9778

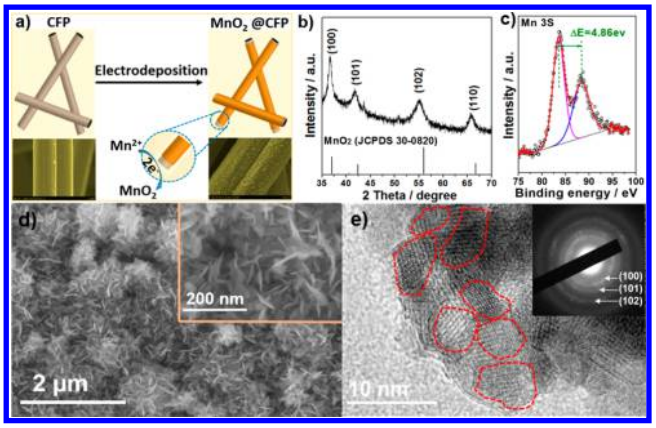

Figure 1. Electrodeposition of MnO_2 on (CFP) and corresponding materials characterization. (a) Schematic illustration of the nanocrystalline MnO_2 electrodeposited on CFP process, and the corresponding SEM images of CFP before and after electrodeposition. Materials characterization of the electrodeposited MnO_2@CFP: (b) XRD pattern; (c) Mn 3S region of the XPS spectra, (in the fitted XPS spectra: black circle, experimental data; red line, overall fitted data; other color lines, fitted individual components); (d) representative SEM image, inset showing the high-magnified SEM; (e) HRTEM image, inset showing the corresponding SAED pattern.

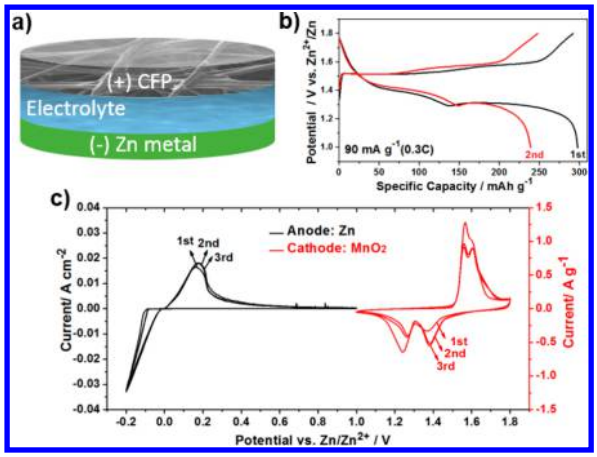

Figure 2. Zn/MnO_2@CFP aqueous batteries design: (a) schematic illustration of the Zn/CFP cell in $ZnSO_4$+$MnSO_4$ aqueous electrolyte before MnO_2 deposited on CFP; (b) galvanostatic charge and discharge curves of the Zn/MnO_2@CFP coin cell at 0.3 C between 1.0 and 1.8 V; (c) cyclic voltammetric (CV) curves of the Zn anode and MnO_2@CFP cathodes in a three-electrode cell using 2 M $ZnSO_4$+0.2 M $MnSO_4$ aqueous electrolyte at 0.5 mv s^{-1}. A small piece of metallic Zn foil was used as the reference electrode in the three-electrode cell.

has a charge state of ~4.0.[9] The SEM images with different magnification (Figure S3) show that the entire surface of the CFP is conformally covered by MnO_2. The corresponding elemental mapping confirms that the surface of CFP is covered by nanostructured MnO_2 (Figure S4). In addition, the high-magnified SEM images further reveal that the MnO_2 was composed of interconnected nanoflakes forming a highly porous structure (Figure 1d). The nanocrystalline and porous feature of MnO_2 also provides abundant electrode/electrolyte contact interfaces and reduces ion diffusion path enabling fast electrochemical kinetics. As the typical TEM images shown in Figure 1e and Figure S5, the MnO_2 nanoflakes are polycrystalline consisting of nanograins with a typical size in the range of 10 nm (highlighted by cycles in Figure 1e). The SAED pattern are well assigned to the (100), (101), and (102) planes of Akhtenskite MnO_2, which are consistent with the XRD results.

Figure 2a shows the "MnO_2 cathode-free" cell design that consists of the Zn metal plate as the anode, $ZnSO_4$+$MnSO_4$ solution as the electrolyte, and the CFP as the cathode current collector. The cell was first galvanostatically charged at 200 μA cm^{-2} to 1.8 V (vs Zn/Zn^{2+}) and then maintained at 1.8 V for 8 h in 2 M $ZnSO_4$+0.2 M $MnSO_4$ electrolyte to obtain the best electrochemical performance after carefully screening a various of electrodeposition protocols (Figure S6 and S7). As shown in Figure 2b, the typical Zn/MnO_2@CFP battery can achieve a discharge capacity of 290 mAh g^{-1} at a current density of 90 mA g^{-1} between 1.0 and 1.8 V in 2 M $ZnSO_4$+0.2 M $MnSO_4$ electrolyte, which is considered as the maximum discharge capacity to define 1 C rate as 290 mA g^{-1}. And the discharge curves in both the first and second cycle show sloping plateaus at ~1.4 V followed with the long flat plateau at around 1.3 V. The overpotential difference is quite small during the first two cycles. The commercial α-MnO_2 also shows two plateaus but both are very sloping due to large α-MnO_2 particle size (Figure S8). The two plateau charge/discharge curves are observed in both electrodeposited MnO_2 and commercial α-MnO_2, which is in good agreement with previous reports.[5c,6,8a,10] The high structural reversibility of electrodeposited MnO_2 during charge/discharge cycles is confirmed by ex situ XRD (Figure S9), where the characteristic peaks of the fully recharged cathode are the same with pristine electrodeposited MnO_2@CFP electrode.

The behaviors of Zn plating/striping and ion insertion/extraction MnO_2 electrode were also evaluated by cyclic voltammetric (CV) in a three-electrode cell using two Zn metal plates as both counter and reference electrode in 2 M $ZnSO_4$+0.2 M $MnSO_4$ aqueous electrolyte (pH value: 4.97). As shown in Figure 2c, the plating/stripping of Zn is stable with almost overlapped CV curves. For MnO_2 cathode, two well separated reversible redox peaks can be clearly observed, corresponding to a two-step reaction. Besides, the CVs of MnO_2@CFP cathode remain invariable after the initial cycle, demonstrating the good reversibility.

The cycling stability and Coulombic efficiency of the Zn/MnO_2@CFP cell at 6.5 C are presented in Figure 3a. After a

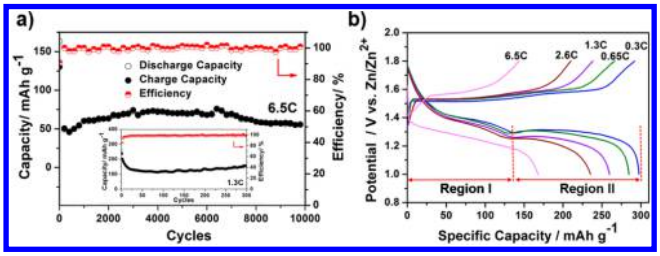

Figure 3. Electrochemical performance of the Zn/MnO_2@CFP cell in 2 M $ZnSO_4$+0.2 M $MnSO_4$ electrolyte: (a) cycling performance and the corresponding Coulombic efficiency at rates of 6.5 C, and 1.3 C (inset); (b) charge and discharge curves at different rates in first cycle.

few conditioning cycles, MnO_2@CFP cathode shows a stable capacity of 50−70 mAh g^{-1} at 6.5 C for 10000 cycles, reaching a high Coulombic efficiency of nearly 100%. At a low rate of 1.3 C (inset in Figure 3a), the MnO_2@CFP cathode delivers an initial discharge capacity of 260 mAh g^{-1} and maintains 150 mAh g^{-1} after 20 cycles. Besides, the high capacity of 290 mAh g^{-1} at 0.3 C is close to the theoretical capacity of MnO_2 (308

DOI: 10.1021/jacs.7b04471
J. Am. Chem. Soc. 2017, 139, 9775−9778

mAh g^{-1}, based on molecular weight of MnO_2 and 1 e^- transfer reaction), demonstrating a high utilization of MnO_2 active material (Figure S10). These superior cycling performances are due to the highly porous nanoflakes feature and their intimate interfacial adhesion to the conductive CFP matrix. The typical SEM images of MnO_2@CFP cathode after 1, 2, 100, and 300 cycles are presented in Figure S11, showing that the nanostructured MnO_2 morphology is essentially preserved on carbon fibers matrix after 300 cycles. Even after the repeated Mn^{2+} dissolution and redeposition process (discharge/charge reaction), the porous nanoflake feature is maintained throughout the cell life. In addition, the EIS results at 1, 2, and 100 cycles are almost overlapped (Figure S12), indicating that the charge transfer resistances of the Zn/MnO_2@CFP cells are remarkably stable during cycling.

The charge and discharge curves of the Zn/MnO_2@CFP cells at different rates in first cycle are shown in Figure 3b. When the charge and discharge rate increase from 0.3 to 6.5 C, about 60% of the capacity at 0.3 C could be preserved, demonstrating the excellent rate capability. Interestingly, with the increase in charge and discharge rate, the voltage and capacity drops in the first voltage plateau (region I) are very small, whereas both the voltage and capacity in the second voltage plateau (region II) significantly dropped, demonstrating that the reaction kinetics in the first (high) plateau is extremely faster than the reaction in the second (low) plateau. At a high rate of 6.5 C, the reaction in the second plateau only contributes less than 20% of the total capacity. This significant difference in kinetic between the two reaction regions could also be observed by the CV sweeps in varied rates. As presented in Figure S13, with the increase in CV sweep rate, the peak I at high voltage (corresponding to reaction in region I) remain obvious whereas the peak II at low voltage (corresponding to the reaction in region II) gradually decay.

The reaction mechanism of MnO_2@CFP cathode in two plateaus was further investigated using GITT and EIS. Figure 4a shows the voltage response of the MnO_2@CFP cathode in GITT measurement. As expected, the total overvoltage in region I is only 0.08 V, which is almost 10 times less than that in region II (0.6 V), but the equilibrium voltage of reaction in region II is just slightly lower than that in the reaction in region I. In GITT, the voltage jump instantly after applying current is due to the ohm and charge transfer resistances, while the gradual voltage change after the discharge is mainly attributed to the ion diffusion.[11]The large overvoltage in region II is attributed to both large voltage jump and slow ion diffusion.

To separate the resistance of ohm, charge transfer, and ion diffusion, EIS is applied on MnO_2@CFP cathode at four different compositions in region I and II marked in Figure 4a, and the results are shown in Figure 4b. The two EISs in the same region are quite similar, whereas the EISs in different regions are largely different. Because the composition difference from 1 to 2, and from 3 to 4 are the same from 2 to 3, the large EIS difference between 2 to 3 (in two region) is not due to the composition difference. After careful examination of the EIS, we found the ohm resistance in both regions are the same, while the charge transfer and diffusion resistance in the region II is much larger than that in region I. Because the interface of MnO_2@CFP to electrolytes are the same in two regions and the composition difference in two regions has neglect impact on the impedance, the significant resistance difference of charge transfer and diffusion in region I and II should be attributed to different ion insertion. Considered the much smaller size of H^+

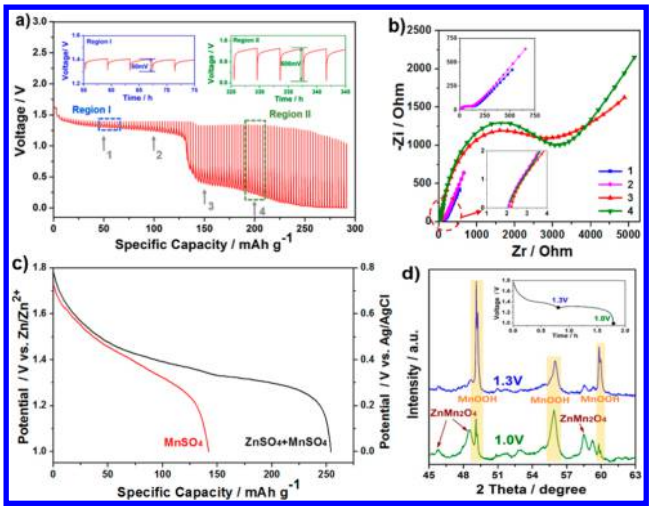

Figure 4. Investigation of reaction mechanism of the MnO_2@CFP cathode during discharge: (a) Discharge galvanostatic intermittent titration technique (GITT) profiles of the Zn/MnO_2@CFP cell (50 mA g^{-1} for 120 s followed by a 4 h rest). (b) Corresponding electrochemical impedance spectroscopy (EIS) at different depth of discharge as indexed by four arrows in panel a. The lower inset shows the magnified region dotted by circle, and the upper inset shows the magnified EIS at 1 and 2. (c) Discharge curves of MnO_2@CFP cathode in 0.2 M $MnSO_4$ solution with or without $ZnSO_4$ as electrolytes at 0.3 C between 0 and 0.8 V (vs Ag/AgCl) in a three-electrode cell. The three-electrode cell use Pt metal as a counter and the Ag/AgCl electrode as a reference, and the potential has been converted to Zn/Zn^{2+} reference for convenience. (d) Ex situ XRD patterns of the MnO_2@CFP cathode at depth of discharge at 1.3 and 1.0 V, respectively.

than Zn^{2+} and the fact that both H^+ and Zn^{2+} ions can be inserted into MnO_2 as reported before,[5−7] it is highly possible that the voltage plateau in region I is due to the H^+ insertion, whereas the voltage plateau in region II is mainly attributed to the Zn^{2+} insertion.

This hypothesis is further confirmed by the electrochemical behaviors comparison of the MnO_2@CFP cathode in 0.2 M $MnSO_4$ electrolytes with or without $ZnSO_4$. As shown in Figure 4c, the discharge curve of MnO_2@CFP electrodes in Zn^{2+}-contained electrolyte using the three-electrode cell displays two different plateaus at ∼1.4 and 1.3 V, consistent with that of Zn/MnO_2@CFP coin cell (Figure 2b). In the Zn^{2+}-absent electrolyte (pH value: 6.53, Table S1), only one sloped plateau from 1.8 to 1.35 V is demonstrated, indicating that the H^+ insert reaction still happened and the first slopping plateau could be undoubtedly ascribed to the H^+ insertion. In contrast, the flat plateau at 1.3 V in region II disappeared due to the absence of Zn^{2+}, which proved that main reaction in region II is contributed by the Zn^{2+} insertion. In addition, MnO_2 only provided a very small capacity (capacitor behavior) in the nonaqueous Zn-ion electrolyte, whereas a significant increase in capacity was observed after adding 1 wt % H_2O in the nonaqueous electrolyte (Figure S14), further confirming that the insertion of Zn^{2+} happens after the H^+-insertion.

Ex situ XRD measurements were conducted on MnO_2@CFP electrode after discharge to 1.3 and 1.0 V inset of Figure 4d) and maintained at 1.3 and 1.0 V for 24 h to identify the equilibrium phase in regions I and II. As shown in Figure 4d, Figure S15 and S16, typical MnOOH peaks are observed after discharge to 1.3 V due to the H^+ insertion. The naked protons insertion rather than hydronium ions insertion in the initial

DOI: 10.1021/jacs.7b04471
J. Am. Chem. Soc. 2017, 139, 9775−9778

discharge process of MnO_2 was also confirmed by the smaller weight loss of the discharged MnO_2 electrode than that of MnOOH during the thermal gravimetric analysis (TGA) in Figure S17. However, the $ZnMn_2O_4$ diffraction peaks can be observed only when the electrode is further discharged to 1.0 V and maintained at 1.0 V for 24 h. The consecutive appearance of the MnOOH and $ZnMn_2O_4$ strongly supports the mechanism that the MnO_2@CFP cathode experience H^+ insertion followed by Zn^{2+} insertion. The Zn insertion was also confirmed by the element mapping in Figure S18.

In conclusion, the consequent H^+ and Zn^{2+} insertion mechanism in Zn/MnO_2 battery chemistry has been first demonstrated by electroanalytical technology combined with XRD, SEM, and TEM using in situ electrodeposited nanocrystal MnO_2 cathode. The highly reversible Zn/MnO_2 battery using in situ deposited MnO_2 on CFP can work stable up to 10 000 cycles at 6.5 C with a low capacity decay rate of 0.007% per cycle. The in situ formed Zn/MnO_2 battery with exceptional performance will simplify the battery fabrication process and reduce cost, providing a new opportunity for next generation of Zn/MnO_2 batteries.

■ ASSOCIATED CONTENT

Supporting Information

The Supporting Information is available free of charge on the ACS Publications website at DOI: 10.1021/jacs.7b04471.

Expermetal details and data (PDF)

■ AUTHOR INFORMATION

Corresponding Authors

*cswang@umd.edu

*memzhu@scut.edu.cn

ORCID

Chongyin Yang: 0000-0002-7127-3087

Min Zhu: 0000-0001-5018-2525

Chunsheng Wang: 0000-0002-8626-6381

Author Contributions

‖W.S. and F.W. contributed equally.

Notes

The authors declare no competing financial interest.

■ ACKNOWLEDGMENTS

The authors acknowledge the financial support of DOE ARPA-E (DEAR0000389) and the technical support of the Nano-Center at the University of Maryland. We thank Dr. Karen J. Gaskell for her valuable comments. Wei Sun was supported by a fellowship from China Scholarship Council (201506150044).

■ REFERENCES

(1) (a) Tarascon, J. M.; Armand, M. *Nature* **2001**, *414*, 359. (b) Goodenough, J. B.; Park, K. S. J. *J. Am. Chem. Soc.* **2013**, *135*, 1167. (c) Lu, Y.; Goodenough, J. B.; Kim, Y. J. *J. Am. Chem. Soc.* **2011**, *133*, 5756.

(2) (a) Li, W.; Dahn, J. R.; Wainwright, D. S. *Science* **1994**, *264*, 1115. (b) Grey, C. P.; Tarascon, J. M. *Nat. Mater.* **2017**, *16*, 45. (c) Suo, L.; Borodin, O.; Gao, T.; Olguin, M.; Ho, J.; Fan, X.; Luo, C.; Wang, C.; Xu, K. *Science* **2015**, *350*, 938. (d) Suo, L.; Borodin, O.; Sun, W.; Fan, X.; Yang, C.; Wang, F.; Gao, T.; Ma, Z.; Schroeder, M.; von Cresce, A.; Russell, S. M.; Armand, M.; Angell, A.; Xu, K.; Wang, C. *Angew. Chem.* **2016**, *128*, 7252. (e) Wang, F.; Suo, L.; Liang, Y.; Yang, C.; Han, F.; Gao, T.; Sun, W.; Wang, C. *Adv. Energy Mater.* **2017**, *7*, 1600922. (f) Wang, F.; Lin, Y.; Suo, L.; Fan, X.; Gao, T.; Yang, C.; Han, F.; Qi, Y.; Xu, K.; Wang, C. *Energy Environ. Sci.* **2016**, *9*, 3666. (g) Li, H.; Wang, Y.; Na, H.; Liu, H.; Zhou, H. J. *J. Am. Chem. Soc.* **2009**, *131*, 15098.

(3) (a) Kundu, D.; Adams, B. D.; Duffort, V.; Vajargah, S. H.; Nazar, L. F. *Nat. Energy* **2016**, *1*, 16119. (b) Winter, M.; Brodd, R. J. *Chem. Rev.* **2004**, *104*, 4245. (c) Cheng, F. Y.; Chen, J.; Gou, X. L.; Shen, P. W. *Adv. Mater.* **2005**, *17*, 2753.

(4) (a) Shen, Y.; Kordesch, K. J. *J. Power Sources* **2000**, *87*, 162. (b) Alfaruqi, M. H.; Gim, J.; Kim, S.; Song, J.; Jo, J.; Kim, S.; Mathew, V.; Kim, J. J. *J. Power Sources* **2015**, *288*, 320.

(5) (a) Xu, C.; Li, B.; Du, H.; Kang, F. *Angew. Chem., Int. Ed.* **2012**, *51*, 933. (b) Zhang, N.; Cheng, F.; Liu, Y.; Zhao, Q.; Lei, K.; Chen, C.; Liu, X.; Chen, J. *J. Am. Chem. Soc.* **2016**, *138*, 12894. (c) Pan, H.; Shao, Y.; Yan, P.; Cheng, Y.; Han, K. S.; Nie, Z.; Wang, C.; Yang, J.; Li, X.; Bhattacharya, P.; Mueller, K. T.; Liu, J. *Nat. Energy* **2016**, *1*, 16039.

(6) (a) Lee, B.; Lee, H. R.; Kim, H.; Chung, K. Y.; Cho, B. W.; Oh, S. H. *Chem. Commun.* **2015**, *51*, 9265. (b) Alfaruqi, M. H.; Mathew, V.; Gim, J.; Kim, S.; Song, J.; Baboo, J. P.; Choi, S. H.; Kim, J. *Chem. Mater.* **2015**, *27*, 3609. (c) Lee, J.; Ju, J. B.; Cho, W. I.; Cho, B. W.; Oh, S. H. *Electrochim. Acta* **2013**, *112*, 138.

(7) Kim, S. H.; Oh, S. M. *J. Power Sources* **1998**, *72*, 150.

(8) (a) Lee, B.; Yoon, C. S.; Lee, H. R.; Chung, K. Y.; Cho, B. W.; Oh, S. H. *Sci. Rep.* **2015**, *4*, 6066. (b) Zhang, K.; Han, X.; Hu, Z.; Zhang, X.; Tao, Z.; Chen, J. *Chem. Soc. Rev.* **2015**, *44*, 699.

(9) Biesinger, M. C.; Payne, B. P.; Grosvenor, A. P.; Lau, L. W.; Gerson, A. R.; Smart, R. S. C. *Appl. Surf. Sci.* **2011**, *257*, 2717. (b) Huang, M.; Zhang, Y.; Li, F.; Wang, Z.; Hu, N.; Wen, Z.; Liu, Q. *Sci. Rep.* **2015**, *4*, 4518.

(10) Xu, D.; Li, B.; Wei, C.; He, Y.-B.; Du, H.; Chu, X.; Qin, X.; Yang, Q.-H.; Kang, F. *Electrochim. Acta* **2014**, *133*, 254.

(11) Fan, X.; Zhu, Y.; Luo, C.; Suo, L.; Lin, Y.; Gao, T.; Xu, K.; Wang, C. *ACS Nano* **2016**, *10*, 5567.

DOI: 10.1021/jacs.7b04471
J. Am. Chem. Soc. 2017, 139, 9775−9778